Terahertz imaging through emissivity control

Michal Mrnka,[1,*] **Harry Penketh,**[1] **Ian R. Hooper,**[1] **Sonal Saxena,**[1] **Nicholas E. Grant,**[2] **John D. Murphy,**[2] **David B. Phillips,**[1] and **Euan Hendry**[1]

[1]*Department of Physics and Astronomy, University of Exeter, Exeter, EX4 4QL, UK*
[2]*School of Engineering, University of Warwick, Coventry, CV4 7AL, UK*
*m.mrnka@exeter.ac.uk

Electromagnetic radiation in the terahertz (THz) frequency band has unique potential for future communication and imaging applications. However, the adoption of THz technologies is hindered by the lack of cost-effective THz sources. Here we demonstrate a way to generate and control THz radiation, via spatio-temporal emissivity modulation. By patterning the optical photoexcitation of a surface-passivated silicon wafer, we locally control the free-electron density, and thereby pattern the wafer's emissivity in the THz part of the electromagnetic spectrum. We show how this unconventional source of controllable THz radiation enables a form of incoherent computational THz imaging. We use it to image various concealed objects, demonstrating that this scheme has the penetrating capability of other THz imaging approaches, without the requirement of femtosecond pulsed laser sources. Furthermore, the incoherent nature of thermal radiation also ensures the obtained images are free of interference artifacts. Our spatio-temporal emissivity control could enable a family of long-wavelength structured illumination, imaging, and spectroscopy systems.

1. INTRODUCTION

All bodies above absolute zero temperatures are sources of electromagnetic radiation described by Planck's law [1]. The total radiated power is given by the thermodynamic temperature of the object T and its emissivity ε, a material parameter that represents its capacity to emit thermal radiation. Dynamic control of thermal radiation has been a very active research area in infrared spectral bands, with a straightforward concept: if one can find a way to spatially or temporally modulate either the temperature or the emissivity, one can then control the radiated power in space and time [2–5]. Control of thermal emission has been achieved with temperature modulation [6,7], dynamic modulation of emissivity in bulk [8,9], and meta-materials [2,10] using visible and ultra-violet (UV) light [2] and electrical modulation [11–13], and using magnetic [14] or thermal [15] fields. In the infrared (IR) band, this approach has led to super-Planckian emitters [16], control of polarization [6,17,18], control of thermal transport [19], new forms of IR camouflage [20–23], radiative cooling [24], thermography [25], and holography [26].

The majority of these approaches are naturally optimized for modulation of mid-infrared thermal radiation, corresponding to peak thermal emission at room temperature for most materials. At the same time, it is appealing to develop thermal modulation approaches for the problematic far-infrared (i.e., THz) region of the spectrum ($\sim 0.3 - 3$ THz) where very few competing technologies exist. Selective generation, control, and detection of THz radiation continues to be technologically challenging, with most

approaches still relying on the generation and detection of THz radiation by high-power or femtosecond lasers [27]. This is despite a broad range of prospective imaging and measurement applications lying in wait, stretching from medicine [28], security [29], and quality control [30] to agriculture [30] and semiconductor industries [31].

In this paper, we present the first experimental demonstration of spatio-temporal control of thermal emission and detection in the THz frequency band. We utilize illumination by structured visible light to induce spatio-temporal modulation of the non-equilibrium free-electron and hole densities in passivated silicon. For rapid modulation of THz emissivity, semiconductors are the natural choice, as free-electron densities can be photo-modulated, while $\sim$THz plasma frequencies typically give rise to large thermal emissivity in the THz range. This brings about local modulation of the emissivity, with a spatial resolution determined by the diffusion length of photocarriers. An essential feature of our new approach is the surface passivation of the silicon, which dramatically enhances the emissivity photomodulation in the THz spectral range. Using a single detector for the emitted thermal radiation and a sequence of orthogonal illumination patterns, we demonstrate a new incoherent THz imaging method that harnesses this control of thermal emission, by reconstructing THz transmittance images of objects placed in the vicinity of the silicon modulator, without the need for any external THz source. As the photomodulation of thermal emission is maximal in the lower THz band, i.e., below 1.5 THz, this approach can be used to image concealed objects

undetectable with visible light, and with a resolution unattainable using microwave radiation.

2. RESULTS

A. Imaging Concept and Experimental Setup

A simplified schematic of our experimental setup is shown in Fig. 1(a). A visible beam of wavelength 623 µm, generated by an LED, is spatially and temporally patterned by a digital micromirror device (DMD) with small individually controllable mirrors. The DMD chip is imaged onto a surface-passivated, high-resistivity silicon wafer. The visible light beam with photon energy above the band gap of silicon generates free electron–hole pairs, which locally modulates the emissivity and thus allows generation of patterned THz radiation necessary for the subsequent computational imaging. Note that using a DMD for this spatial multiplexing is superior to raster scanning by allowing a distribution of the optical intensity over the modulator, thereby circumventing saturation (an effect discussed in Section 3.C). The right side of Fig. 1(a) shows how the contrast between the illuminated and unilluminated areas is created—each small illuminated region behaves like a local Lambertian source with the maximum power radiated in the direction normal to the wafer.

An object to be imaged is placed close to the surface-passivated wafer. We mount a thin, thermally insulating layer (of thickness ≈200 µm) in between the object and the wafer to prevent conductive heating of the object. The thermal radiation emitted by the wafer is transmitted through the object and collected by a large 90° offset aluminium paraboloid mirror with an effective focal length of 101.6 mm and an equally large diameter. The numerical aperture (NA) of the system on the object side of the mirror is NA = 0.2 resulting in a diffraction limited spot size of 0.75 mm at 1 THz. The THz radiation transmitted through the object is collected by the mirror and coupled to an $f/2$ Winston cone with 25 mm diameter through two low-pass optical filters to reject radiation above 1.5 THz. The aperture of the Winston cone is located at a plane conjugate to the plane of the wafer. Inside a He cryostat, the Winston cone is followed by an InSb bolometer, with detection frequency bandwidth of 0.06–1.5 THz and response time of 350 ns. The signal from the detector is amplified by a low-noise electronic amplifier. A 3 kHz electronic low-pass filter is used to reduce the instantaneous bandwidth to better suit our imaging rates while suppressing the noise level. In the experiments, we apply a small tilt of 15° to the wafer to redirect the specular reflection toward a room temperature absorber instead of the detector itself, which prevents unwanted artifacts (see Supplement 1, Section 8). The temporal voltage signal is digitized with an analogue-to-digital converter, and the signal collected for a sequence of different patterned visible beams enabling the image to be reconstructed with a superior signal-to-noise ratio compared to raster scanning or focal plane
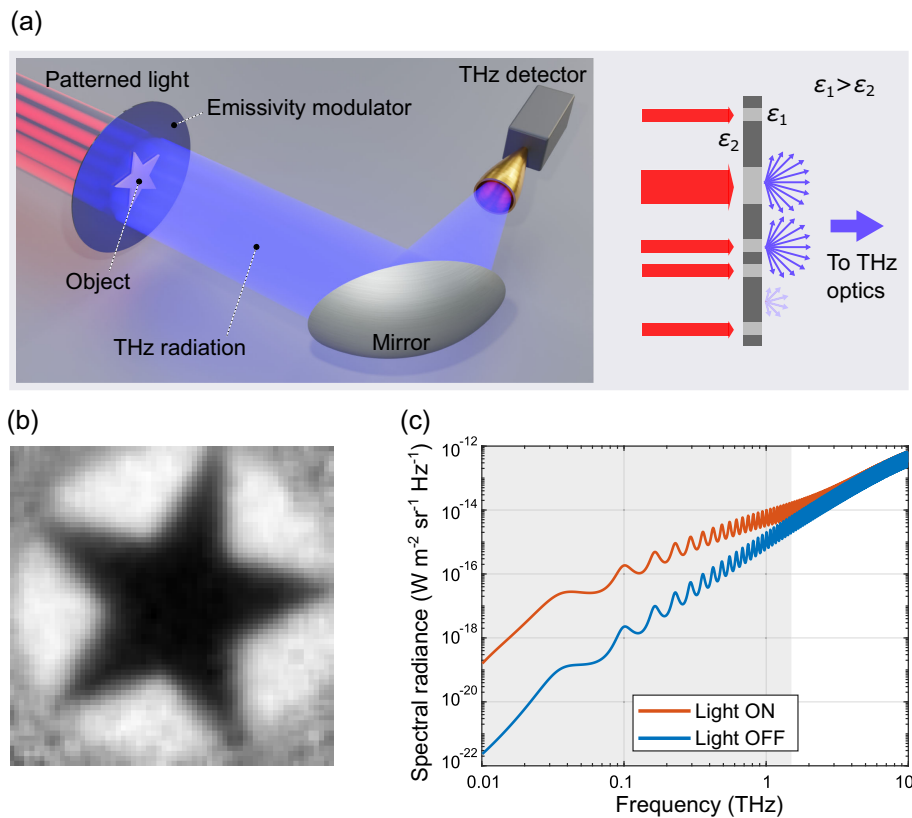

Fig. 1. Principle and experimental setup. (a) A spatially patterned visible light beam illuminates a silicon wafer from one side. The structured terahertz beam generated by the modulated emissivity of the wafer ε (on the right) interacts with the object and is collected by the large offset parabolic mirror to be focused onto a single-pixel detector. (b) Measured image of a conductive object; low brightness corresponds to low THz transmission. (c) Simulated spectral radiance of the passivated silicon wafer with 675 µm thickness and 0.36 ms effective carrier lifetime at 24°C temperature. The red and blue curves correspond to the radiances with and without applying a photoexcitation light intensity of 200 W/m². Note that the increased spectral radiance resulting from photoexcitation primarily occurs due to an increased emissivity, though there is also a smaller heating effect on photoexitation, as the modulator temperature increases by 5°C over the environment, determined experimentally. The difference between these curves gives rise to the photomodulation efficiency. The gray area corresponds to the spectral range of our detector.

arrays [see Supplement 1, Section 11 for details on the method and Fig. 1(b) for an example image].

B. Emissivity Modulation

The key to achieving THz imaging through emissivity control is the design of our THz photo-modulator. In the experiment, the patterned visible beam illuminates a 675 µm thick, high-resistivity, undoped silicon wafer engineered with a ZnO/Al_2O_3 surface passivation layer stack. This passivation reduces the surface recombination velocity of generated free carriers, which therefore increases the effective charge carrier lifetime τ_{eff} from ≈ 0.022 ms (unpassivated) to ≈ 0.36 ms (passivated) [32,33]. We note that without the Al_2O_3 capping layer, ZnO does not provide sufficient passivation to have any impact on the modulation efficiency. In this case the Al_2O_3 layer provides a source of hydrogen [34] that enables improved surface passivation and an optimal effective lifetime of ≈ 0.36 ms. The level of passivation given by ZnO/Al_2O_3 was thus appropriate here as it enables intermediate lifetimes to be reached between unpassivated and excellent surface passivation given by Al_2O_3 alone. The cross section of the wafer is given in Supplement 1, Fig. S4 and a detailed description of its fabrication in Supplement 1, Section 10.

When light illuminates the wafer, photo generated electron–hole pairs modify the permittivity of the material. This in turn renders the modified silicon wafer an efficient absorber/emitter in the millimeter and lower terahertz bands via an increase in the plasma frequency of the electrons and holes (see Supplement 1, Section 2). The high effective carrier lifetime in the passivated wafer provides a substantial increase in emissivity at terahertz frequencies under a modest illumination intensity (≈ 100 s of Watts per m²)—see Fig. 1(c), where the spectral radiance $B(\nu, T)$ is calculated according to Supplement 1, Section 2, and ν is the temporal frequency. The spectral radiance expected for a silicon wafer with a 0.36 ms effective carrier lifetime is plotted for two cases: with and without photoexcitation intensity of 200 W/m², corresponding to electron densities of $6.38 \cdot 10^{20}$ m⁻³ and $1.45 \cdot 10^{16}$ m⁻³, respectively. The emission peaks in Fig. 1(c) correspond to Fabry–Pérot resonances, and are calculated for emission normal to the wafer. Note that since we have a collection angle of $\pm 11.5°$ (NA = 0.2), and these peaks shift with angle, they will be diminished in the experiment. As the emissivity modulation depth is proportional to the difference between the radiance of the photoexcited and non-photoexcited silicon, the useful spectral range of the emission approximately coincides with the spectral range of the detector [gray area in Fig. 1(c)].

In order to make the THz thermal emission observable under room temperature conditions (see Section 3.B) and to further boost its level, we increase the thermodynamic temperature of the modulator to 120°C. We accomplish this by heating the wafer by convection using a heat gun facing the illuminated face of the wafer. We use thermocouple devices on both sides to monitor the temperature gradient across the device. We observe that the emission signal increases with increasing temperature almost linearly, as expected by the Rayleigh–Jeans law (see Fig. 2). Kirchhoff's law explains why heating is required to increase signals (see Supplement 1, Section 4).
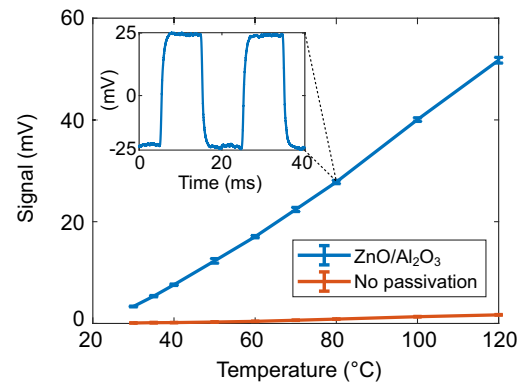

Fig. 2. Thermal emission enhancement via surface passivation. Measured signal level as a function of wafer temperature for the ZnO/Al_2O_3 passivated wafer with a room temperature carrier lifetime $\tau = 0.36$ ms and for the unpassivated wafer with $\tau = 0.022$ ms. The on/off photoexcitation is applied with intensity of 300 W/m². Inset shows the modulated signal sampled in time for the passivated wafer. The measured signal level corresponds to the amplitude of the spectral component at the modulation frequency.

C. Imaging

We image several different objects under a photoexcitation intensity of 200 W/m². Figures 3(a)–3(c) show images of a copper etched Siemens star deposited on a thin plastic film and placed ≈ 200 µm away from the wafer, chosen to test the imaging resolution of our technique. The THz image is normalized to an image taken without the sample present under the same conditions. Dark regions of the image correspond to areas with low THz transmission—in this case shielded by copper. The size of the full field of view of the system is 27×27 mm². Here we set the pixel size to 0.42×0.42 mm² (controlled by how many DMD micro-mirrors are binned into a single super-pixel. The minimum discernible feature in the image is about 1.2 mm [see the red arrows in Fig. 3(b)], limited by free-charge diffusion in the wafer.

One of the main advantages of terahertz radiation is its ability to penetrate through certain visibly opaque materials such as paper, plastics, and ceramics. Here, we demonstrate that our system is sensitive enough to take advantage of this capability, by imaging two hidden objects shown in Figs. 3(d)–(g): a razor blade in a paper envelope and a commercial radio frequency identification (RFID) tag sandwiched between a plastic and a paper layer. For noise suppression, we apply a simple 2D sliding average filter with a mask size of 3×3 pixels—every pixel in the final images is thus a mean value of 3×3 neighboring pixels from the original image. The circular copper wiring with outside diameter of 22 mm, and the chip inside of the wiring, are both opaque for the terahertz radiation, while the plastic cover of the tag is mostly transparent at these frequencies. The two narrow leads connecting the chip and the wiring can be faintly recognized in the upper left-hand corner of the tag.

3. DISCUSSION

A. Effects of Carrier Lifetime and Diffusion

One of the key considerations in this work is the optimization of the emissivity photomodulator. There are competing constraints that lead to a trade-off between different aspects of device performance. To achieve optimal image resolution, a short carrier lifetime
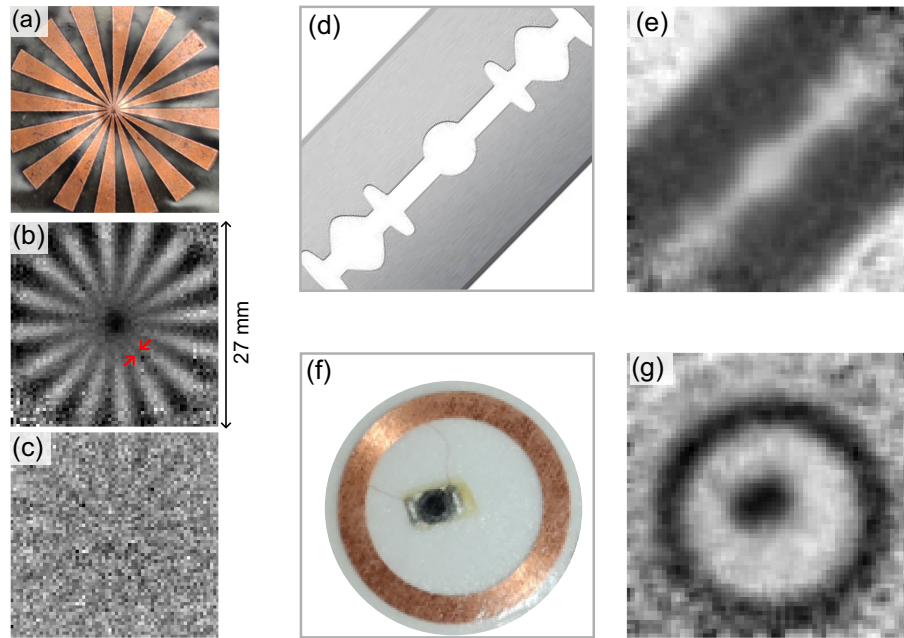
Fig. 3.   Imaging with the emissivity modulator. (a)–(c) Images of a Siemens star resolution target. Optical (a) and terahertz (b) images, the latter reconstructed with our ZnO/Al$_2$O$_3$ passivated wafer. For comparison, image (c) is measured using an unpassivated high-resistivity silicon wafer. Red arrows in (b) highlight the smallest resolvable feature, estimated to be 1.2 mm. (d)–(g) Optical images of a razor blade (d) and an uncovered radio frequency identification tag (f); (e) and (g) show our THz images of these objects concealed inside a paper envelope.

should be prioritized. This is because image resolution is currently determined by carrier diffusion length $L = \sqrt{D\tau_{\text{eff}}}$, where D is the diffusion coefficient of charge carriers. By engineering a wafer with a longer effective lifetime we trade a shorter integration time for a lower image resolution (see Supplement 1, Section 4). We can see that the resolution in Fig. 3(b) (which is estimated as 1.2 mm) is notably lower compared to the diffraction limit (0.75 mm at 1 THz) and agrees with the expected diffusion length of electrons of 1.1 mm for a carrier lifetime of 0.36 ms.

However, there is simultaneously a stringent trade-off between imaging time and image resolution in our approach. A significantly shorter carrier lifetime results in a much lower modulation of emissivity for the same optical power. For comparison, in Fig. 3(c) we show an image with an unpassivated 22 μs effective lifetime wafer, taken under the same conditions as Fig. 3(b). Furthermore, the fact that the signal increases with the increasing carrier lifetime (see Fig. 2 and Supplement 1, Section 4) demonstrates that it is the modulated emissivity and not temperature that gives rise to the increased thermal emission on photoexcitation.

A carrier lifetime of $\tau_{\text{eff}} \approx 0.36$ ms allows us to implement a 10 ms pattern projection time for each optical pattern, resulting in an imaging time of approximately 41 s for 64 × 64 pixels. However, in our proof-of-principle experiments, in order to reduce image noise, averaging over much longer times is currently required: the images in Figs. 3(b) and 3(c) were integrated for 176 min, and images in Figs. 3(e) and 3(g) were integrated for 44 min.

Finally, we note that Caratenuto *et al*. [14] recently published simulation results that suggest that modulation of thermal THz radiation is feasible using a high magnetic field applied to an InSb based metamaterial to tune a THz emissivity resonance. However, it is not clear how an approach relying on high magnetic fields can be extended to spatially varying control or how fast modulation may be achieved.

B. Heating the Modulator

Kirchhoff's law explains why heating of the modulator is necessary, and why the change in emissivity of a room temperature wafer is not sufficient to generate any observable signal: at room temperature, under thermal equilibrium conditions, the radiation absorbed by the modulator from the environment is exactly balanced by the radiation emitted by the modulator itself. It follows that, in the event of an emissivity increase in the modulator, any additional radiation thermally emitted by the modulator itself is exactly offset by a reduction in the transmission/reflection of radiation from the environment due to an increased absorption of the modulator. It is only when the temperature of the modulator is elevated with respect to the environment that the modulation in the emitted radiation is measurable. Due to the limited heating capabilities of our setup, the maximum modulator temperature we could achieve was 120°. However, further increases in the emission are expected if this temperature difference is increased.

C. Outlook

The protracted integration times used here are a current limitation of our setup. However, we note that there are many routes to improvement that would lead to a competitive and/or cost effective THz imaging system using our approach. In this section we discuss the various trade-offs to consider.

In general, the routes for improvement can be analyzed by examining the signal-to-noise ratio, defined for our imaging system as

$$\frac{S}{N} = \frac{P_{\text{in}}}{\text{NEP}} \sqrt{2 \cdot \Delta t_{\text{int}}}, \tag{1}$$

where the detector noise equivalent power is NEP, and the received power is given by

$$P_{\text{in}} = \int_A \int_\Omega \int_{\Delta\nu} \Delta\varepsilon(\nu, \tau_{\text{eff}}, I) \cdot B_{\text{bb}}(\nu, T) \mathrm{d}\nu \mathrm{d}\Omega \mathrm{d}A, \qquad (2)$$

where A, Ω, and $\Delta\nu$ represent the area of the photoexcited modulator (i.e., the field of view), solid angle of the optics, and temporal frequency range of the detector, respectively. $\Delta\varepsilon$ is the change in emissivity upon photomodulation, and B_{bb} corresponds to the spectral radiance of an ideal black body at temperature T. Equation (1) tells us that the integration time Δt_{int} is expected to be proportional to $(\text{NEP})^2$ and inversely proportional Ω^2, $\Delta\varepsilon^2$, and $\Delta\nu^2$. Therefore a relatively small decrease in detector NEP, or relatively small increases in the solid collection angle, modulator emissivity change, or detector frequency range will all lead to large decreases in the required integration times.

The detector used in this work has an NEP measured to be $0.13~\text{nW/Hz}^{1/2}$ (see Supplement 1, Section 9). A modest three-fold improvement in NEP would result in almost an order of magnitude improvement in integration time. However, there is a possibility here for even greater improvement, with 4.2 K and 1.6 K bolometers [35] reporting NEPs in the $\text{pW/Hz}^{1/2}$ and $\text{fW/Hz}^{1/2}$ range, respectively, at detection rates compatible with our experiments. With such low detector NEPs, and all other conditions being equal, integration times would drop from tens of minutes to sub-second. Similarly, a detector with a larger frequency range $\Delta\nu$ would also lead to considerable improvements. However, for $\Delta\nu$, one should also consider the frequency range required for a particular application. For example, frequencies in the higher THz bands would not have the penetrative capability exhibited in Fig. 3.

A second route to improvement lies in the collection optics. For this, a small increase in solid collection angle Ω will have a strong effect, dependant on the second power. However, one needs to match the collection angle of the optics to the collection angle of the detector. This is a severe limitation in current commercially available THz bolometers. Furthermore, optics with an additional conjugate plane would remove the requirement on the close alignment of the object with the modulator, as it would allow projection of the generated THz patterns from the modulator onto the object.

A third route is to look to increase the photo-induced emissivity change, $\Delta\varepsilon$. One can do this by increasing the lifetime of photocarriers in the modulator. However, this is rather complicated, as the emissivity change is not independently tuneable in this way, and a longer carrier lifetime will lead to lower imaging resolution due to carrier diffusion, while also decreasing the detection rate. A more straightforward route to increasing $\Delta\varepsilon$ is the photo-optical excitation intensity. For relatively small increases in optical power, we expect $\Delta\varepsilon$ to increase linearly (intensity dependence shown in Supplement 1, Section 5), e.g., a three-fold increase in the optical illumination intensity (I) would yield almost an order of magnitude decrease in integration time. However, there is a limitation to this: for higher-power laser sources, while we expect $\Delta\varepsilon$ to increase with increasing power, Auger recombination will lead to a lower carrier lifetime and saturation of $\Delta\varepsilon$ for optical intensities over $10~\text{kW/m}^2$ [32,36]. Similarly, one can also increase the modulator temperature, which leads to larger values for the function $B_{\text{bb}}(\nu, T)$ in Eq. (1).

Finally, it is interesting to consider the paths towards low-cost, room-temperature THz imaging systems. Cheap, uncooled detectors in the THz range, such as pyroelectric detectors and Golay cells, tend to have high NEPs, typically $>\text{nW/Hz}^{1/2}$. As expected, when we tested our experiment with such a detector, we required integration times of many hours. Therefore, to form a practical imaging system using such a detector, one would simultaneously require increases to the collection angle, optical excitation intensity, and/or modulator temperature to offset the effect of the higher detector NEP.

Alternatively, coherent heterodyne radiometric receivers can be used at these frequencies. Such heterodyne detectors offer superior noise performance at the expense of the reduced instantaneous frequency bandwidth under room-temperature conditions. NEP of the order of $10~\text{pW/Hz}^{-1}$ has recently been achieved with this detector type [37] in nearby frequency bands. While these detectors tend to have relatively narrow frequency ranges (relative bandwidth of $\sim 9\%$ reported in [37]), and small collection angles, an NEP in the pW/Hz^{-1} range should be able to offset bandwidth and collection deficiencies, and may alone outperform the results achieved in our study even with a room-temperature detector.

Furthermore, there is also scope for improving the data collection scheme: if priors about the object under inspection are available, compressive sensing can also be used to reduce the number of patterns that need to be projected, thus enhancing the imaging rate [38]. We therefore emphasize that there is significant scope for future improvement in imaging times with our conceptually new THz imaging approach.

4. CONCLUSIONS

In summary, we have demonstrated a dynamic, all-optical, spatial emissivity modulator at terahertz frequencies based on photomodulation of surface-passivated silicon. We have also proposed and experimentally validated an imaging method that inherently relies on such a modulator, requiring no external THz source. Thanks to the relatively long charge carrier lifetime of our surface-passivated Si wafer, the emissivity modulation required only a modest intensity patterned pump beam ($200~\text{W/m}^2$)—provided by a standard LED source and a digital micromirror device.

We believe our imaging approach has potential to compete with standard THz imaging techniques, overcoming the current dependence on femtosecond lasers for generation and detection in this frequency band. By incorporating suitable optics, it will be also possible to use the thermal emission process studied here for stand-off imaging. Furthermore, by combining thermal emission modulation with microantenna arrays patterned onto the wafer, additional control may be achievable, including over spectral content, directionality [39–43], and polarization state [6,17,18] of the thermally emitted terahertz radiation. These possibilities suggest our thermal modulation approach will find a range of applications beyond imaging.

Author contributions. M.M. and E.H. devised the concept of the modulator and the experiment. M.M. carried out the analytical modeling, data acquisition, and post-processing and wrote the first draft of the manuscript. D.B.P. and H.P. provided support on computational imaging aspects of the project and assisted with the design of the data acquisition software. M.M., E.H., H.P., D.B.P., I.R.H., and S.S. contributed to the interpretation of the experimental data. I.R.H. assisted with the measurements of the effective lifetimes. N.E.G. and J.D.M. designed and fabricated the emissivity modulator. All authors edited the paper.

Disclosures. The authors declare no conflicts of interest.

Data availability. Data underlying the results presented in this paper are not publicly available at this time but may be obtained from the authors upon reasonable request.

Supplemental document. See Supplement 1 for supporting content.

REFERENCES

1. M. Planck, "Ueber das gesetz der energieverteilung im normalspectrum," Ann. Phys. **309**, 553–563 (1901).
2. Z. J. Coppens and J. G. Valentine, "Spatial and temporal modulation of thermal emission," Adv. Mater. **29**, 1701275 (2017).
3. J.-J. Greffet, "Controlled incandescence," Nature **478**, 191–192 (2011).
4. D. G. Baranov, Y. Xiao, I. A. Nechepurenko, A. Krasnok, A. Alù, and M. A. Kats, "Nanophotonic engineering of far-field thermal emitters," Nat. Mater. **18**, 920–930 (2019).
5. M. F. Picardi, K. N. Nimje, and G. T. Papadakis, "Dynamic modulation of thermal emission—a tutorial," J. Appl. Phys. **133**, 111101 (2023).
6. L. Wojszvzyk, A. Nguyen, A.-L. Coutrot, C. Zhang, B. Vest, and J.-J. Greffet, "An incandescent metasurface for quasimonochromatic polarized mid-wave infrared emission modulated beyond 10 MHz," Nat. Commun. **12**, 1492 (2021).
7. N. Li, H. Yuan, L. Xu, Y. Zeng, B. Qiang, Q. J. Wang, S. Zheng, H. Cai, L. Y. T. Lee, N. Singh, and D. Zhao, "Tailorable infrared emission of microelectromechanical system-based thermal emitters with NiO films for gas sensing," Opt. Express **29**, 19084–19093 (2021).
8. Z. Xu, Q. Li, K. Du, S. Long, Y. Yang, X. Cao, H. Luo, H. Zhu, P. Ghosh, W. Shen, and M. Qiu, "Spatially resolved dynamically reconfigurable multilevel control of thermal emission," Laser Photon. Rev. **14**, 1900162 (2019).
9. Y. Xiao, N. A. Charipar, J. Salman, A. Piqué, and M. A. Kats, "Nanosecond mid-infrared pulse generation via modulated thermal emissivity," Light Sci. Appl. **8**, 51 (2019).
10. T. Inoue, M. D. Zoysa, T. Asano, and S. Noda, "Realization of dynamic thermal emission control," Nat. Mater. **13**, 928–931 (2014).
11. S. Vassant, I. M. Doyen, F. Marquier, F. Pardo, U. Gennser, A. Cavanna, J. L. Pelouard, and J. J. Greffet, "Electrical modulation of emissivity," Appl. Phys. Lett. **102**, 081125 (2013).
12. V. W. Brar, M. C. Sherrott, M. S. Jang, S. Kim, L. Kim, M. Choi, L. A. Sweatlock, and H. A. Atwater, "Electronic modulation of infrared radiation in graphene plasmonic resonators," Nat. Commun. **6**, 7032 (2015).
13. J. Park, J.-H. Kang, X. Liu, S. J. Maddox, K. Tang, P. C. McIntyre, S. R. Bank, and M. L. Brongersma, "Dynamic thermal emission control with InAs-based plasmonic metasurfaces," Sci. Adv. **4**, eaat3163 (2018).
14. A. Caratenuto, F. Chen, Y. Tian, M. Antezza, G. Xiao, and Y. Zheng, "Magnetic field-induced emissivity tuning of InSb-based metamaterials in the terahertz frequency regime," Opt. Mater. Express **11**, 3141 (2021).
15. K. Tang, X. Wang, K. Dong, Y. Li, J. Li, B. Sun, X. Zhang, C. Dames, C. Qiu, J. Yao, and J. Wu, "A thermal radiation modulation platform by emissivity engineering with graded metal–insulator transition," Adv. Mater. **32**, 1907071 (2020).
16. Y. Xiao, M. Sheldon, and M. A. Kats, "Super-Planckian emission cannot really be 'thermal'," Nat. Photonics **16**, 397–401 (2022).
17. X. Wang, T. Sentz, S. Bharadwaj, S. K. Ray, Y. Wang, D. Jiao, L. Qi, and Z. Jacob, "Observation of nonvanishing optical helicity in thermal radiation from symmetry-broken metasurfaces," Sci. Adv. **9**, eade4203 (2023).
18. A. Nguyen, J.-P. Hugonin, A.-L. Coutrot, E. Garcia-Caurel, B. Vest, and J.-J. Greffet, "Large circular dichroism in the emission from an incandescent metasurface," Optica **10**, 232–238 (2023).
19. Y. Li, W. Li, T. Han, X. Zheng, J. Li, B. Li, S. Fan, and C.-W. Qiu, "Transforming heat transfer with thermal metamaterials and devices," Nat. Rev. Mater. **6**, 488–507 (2021).
20. C. Xu, G. T. Stiubianu, and A. A. Gorodetsky, "Adaptive infrared-reflecting systems inspired by cephalopods," Science **359**, 1495–1500 (2018).
21. B. Gui, J. Wang, X. Lu, Y. Zhu, L. Zhang, M. Feng, W. Huang, J. Wang, H. Ma, and S. Qu, "Spectrally-switchable infrared selective emitters for adaptive camouflage," Infrared Phys. Technol. **126**, 104363 (2022).
22. Y. Qu, Q. Li, L. Cai, M. Pan, P. Ghosh, K. Du, and M. Qiu, "Thermal camouflage based on the phase-changing material GST," Light Sci. Appl. **7**, 26 (2018).
23. R. Hu, W. Xi, Y. Liu, K. Tang, J. Song, X. Luo, J. Wu, and C.-W. Qiu, "Thermal camouflaging metamaterials," Mater. Today **45**, 120–141 (2021).
24. W. Li and S. Fan, "Nanophotonic control of thermal radiation for energy applications," Optics Express **26**, 15995–16021 (2018).
25. Y. Xiao, C. Wan, A. Shahsafi, J. Salman, and M. A. Kats, "Depth thermography: noninvasive 3D temperature profiling using infrared thermal emission," ACS Photon. **7**, 853–860 (2020).
26. M. Zhou, E. Khoram, D. Liu, B. Liu, S. Fan, M. L. Povinelli, and Z. Yu, "Self-focused thermal emission and holography realized by mesoscopic thermal emitters," ACS Photon. **8**, 497–504 (2021).
27. E. Castro-Camus, M. Koch, and D. M. Mittleman, "Recent advances in terahertz imaging: 1999 to 2021," Appl. Phys. B **128**, 12 (2021).
28. L. Yu, L. Hao, T. Meiqiong, H. Jiaoqi, L. Wei, D. Jinying, C. Xueping, F. Weiling, and Z. Yang, "The medical application of terahertz technology in non-invasive detection of cells and tissues: opportunities and challenges," RSC Adv. **9**, 9354–9363 (2019).
29. R. Appleby and R. N. Anderton, "Millimeter-wave and submillimeter-wave imaging for security and surveillance," Proc. IEEE **95**, 1683–1690 (2007).
30. L. Afsah-Hejri, P. Hajeb, P. Ara, and R. J. Ehsani, "A comprehensive review on food applications of terahertz spectroscopy and imaging," Compr. Rev. Food Sci. Food Saf. **18**, 1563–1621 (2019).
31. J. True, C. Xi, N. Jessurun, K. Ahi, and N. Asadizanjani, "Review of THz-based semiconductor assurance," Opt. Eng. **60**, 060901 (2021).
32. I. R. Hooper, N. E. Grant, L. E. Barr, S. M. Hornett, J. D. Murphy, and E. Hendry, "High efficiency photomodulators for millimeter wave and THz radiation," Sci. Rep. **9**, 18304 (2019).
33. I. R. Hooper, E. Khorani, X. Romain, L. E. Barr, T. Niewelt, S. Saxena, A. Wratten, N. E. Grant, J. D. Murphy, and E. Hendry, "Engineering the carrier lifetime and switching speed in si-based mm-wave photomodulators," J. Appl. Phys. **132**, 233102 (2022).
34. B. W. H. van de Loo, B. Macco, J. Melskens, W. Beyer, and W. M. M. Kessels, "Silicon surface passivation by transparent conductive zinc oxide," J. Appl. Phys. **125**, 105305 (2019).
35. I. B. Systems, 2023, https://www.irlabs.com/products/bolometers/bolometer-systems/.
36. T. Niewelt, B. Steinhauser, A. Richter, B. Veith-Wolf, A. Fell, B. Hammann, N. Grant, L. Black, J. Tan, A. Youssef, J. Murphy, J. Schmidt, M. Schubert, and S. Glunz, "Reassessment of the intrinsic bulk recombination in crystalline silicon," Solar Energy Mater. Sol. Cells **235**, 111467 (2022).
37. J. Kim, D. Yoon, H. Son, D. Kim, J. Yoo, J. Yun, H. J. Ng, M. Kaynak, and J.-S. Rieh, "Terahertz signal source and receiver operating near 600 GHz and their 3-D imaging application," IEEE Trans. Microwave Theory Tech. **69**, 2762–2775 (2021).
38. R. I. Stantchev, D. B. Phillips, P. Hobson, S. M. Hornett, M. J. Padgett, and E. Hendry, "Compressed sensing with near-field THz radiation," Optica **4**, 989–992 (2017).
39. X. Liu, T. Tyler, T. Starr, A. F. Starr, N. M. Jokerst, and W. J. Padilla, "Taming the blackbody with infrared metamaterials as selective thermal emitters," Phys. Rev. Lett. **107**, 045901 (2011).
40. J.-J. Greffet, R. Carminati, K. Joulain, J.-P. Mulet, S. Mainguy, and Y. Chen, "Coherent emission of light by thermal sources," Nature **416**, 61–64 (2002).
41. S. Shin, M. Elzouka, R. Prasher, and R. Chen, "Far-field coherent thermal emission from polaritonic resonance in individual anisotropic nanoribbons," Nat. Commun. **10**, 1377 (2019).
42. X. Zhang, Z. Zhang, Q. Wang, S. Zhu, and H. Liu, "Controlling thermal emission by parity-symmetric Fano resonance of optical absorbers in metasurfaces," ACS Photon. **6**, 2671–2676 (2019).
43. R. Fenollosa, F. Ramiro-Manzano, M. Garn, and R. Alcubilla, "Thermal emission of silicon at near-infrared frequencies mediated by Mie resonances," ACS Photon. **6**, 3174–3179 (2019).